Journal of Sound and Vibration (2000) **230**(3), 541–560
doi:10.1006/jsvi.1999.2628, available online at http://www.idealibrary.com on IDEAL®

SIMULATION OF ACOUSTIC SCATTERING FROM A TRAILING EDGE†

B. A. SINGER, K. S. BRENTNER AND D. P. LOCKARD

Fluid Mechanics and Acoustics Division, NASA Langley Research Center, Hampton, VA 23681-2199, *U.S.A.*

AND

G. M. LILLEY

ICASE, NASA Langley Research Center, Hampton, VA 23681-2199, *U.S.A.*

(*Received* 10 *February* 1999, *and in final form* 2 *August* 1999)

Three model problems were examined to assess the difficulties involved in using a hybrid scheme coupling flow computation with the Ffowcs Williams and Hawkings equation to predict the noise generated by vortices passing over a sharp edge. The results indicate that the Ffowcs Williams and Hawkings equation correctly propagates the acoustic signals when provided with accurate flow information on the integration surface. The most difficult of the model problems investigated flow over a two-dimensional, thin NACA airfoil with a bluff-body vortex generator positioned at 98% chord. Vortices rolled up downstream of the bluff body. The shed vortices possessed similarities to large coherent eddies in boundary layers in that they interacted and occasionally paired as they convected past the sharp trailing edge of the airfoil. The calculations showed acoustic waves emanating from the airfoil trailing edge. Acoustic directivity and Mach number scaling were obtained.

1. INTRODUCTION

In the theory of aerodynamic noise developed by Lighthill [1, 2], turbulent fluctuations in free space are particularly inefficient radiators of noise in a low-speed flow. The turbulent fluctuations are quadrupole-type sources, and hence the radiated acoustic intensity varies as a characteristic velocity scale u to the eighth power. However, when a turbulent eddy passes in the vicinity of a sharp edge of a solid surface, the character of the farfield acoustic radiation changes dramatically, and the turbulent fluctuations radiate much more strongly.

Ffowcs Williams and Hall [3] first investigated this problem by modelling a typical turbulent eddy as a quadrupole point source near the edge of a half-plane.

†Presented as AIAA Paper No. 99-0231 at the 37th Aerospace Sciences Meeting and Exhibit, Reno, Nevada, January 1–14, 1999.

0022-460X/00/080541 + 20 $35.00/0

They found the controlling parameter to be kr_0 where k is the acoustic wavenumber ω/c, ω is the radian acoustic frequency, c is the speed of sound, and r_0 is the distance from the quadrupole to the edge of the half-plane. For quadrupoles having fluid motion in a plane perpendicular to the edge, and for which $2kr_0 \ll 1$, the sound output from the associated quadrupoles increases by a factor of $(kr_0)^{-3}$. With the additional assumptions that the eddy perturbation velocity and the acoustic frequency scale linearly with the characteristic velocity scale u, Ffowcs Williams and Hall [3] found that the acoustic intensity increases by a factor of u^{-3} relative to the case of quadrupoles in free space. This means that a quadrupole noise source in the vicinity of a sharp edge radiates noise proportional to u^5, which for low-Mach-number flows is greater than the u^6 scaling in the case of Curle's [4] surface dipoles for acoustically compact surfaces. Ffowcs Williams and Hall [3] also found that the intensity varies as $\sin^2(\theta/2)$, where θ is the angle measured relative to the downstream extension of the half-plane. Subsequent analysis by Goldstein [5] confirmed the findings of Ffowcs Williams and Hall [3].

Crighton [6] calculated the acoustic field generated by a line vortex passing around the edge of a rigid half-plane by matching the complex potential flow solution with a slightly compressible solution. His results show that the presence of the edge increases the acoustic energy radiated by the vortex by an amount proportional to M^{-3}, where $M \equiv u/c$ is a characteristic Mach number for the flow. This result is consistent with all scattering theories at low Mach number.

Howe [7] reviewed various trailing-edge theories and showed that for low-Mach-number flow they all give essentially the same predictions when properly interpreted. Howe then extended the theory of trailing-edge noise to include the effects of source motion relative to the trailing edge, Doppler-shift, and whether or not an unsteady Kutta condition is applied at the trailing edge. None of his extensions alter the important scaling relations obtained in the original analysis of Ffowcs Williams and Hall [3].

The theoretical predictions were largely supported by the results of the Brooks and Hodgson [8] trailing-edge noise experiments on a NACA 0012 airfoil at low incidence in an anechoic quiet-flow facility. They mounted surface-pressure sensors near the airfoil trailing edge to obtain unsteady surface-pressure data and measured the radiated noise with microphones placed at various angular positions between two and four chord lengths away from the trailing edge. Among other findings, their results confirmed that a turbulent boundary layer on an airfoil with a sharp trailing edge radiates with an acoustic intensity that scales with u^5 and a downstream directivity proportional to $\sin^2(\theta/2)$.

Calculation methods for acoustic fields that include trailing-edge noise currently are largely empirical [9]. In this work we explore the feasibility of directly computing the acoustic field generated by flow over a sharp trailing edge. A hybrid computational approach is taken wherein a commonly used, general purpose Computational Fluid Dynamics (CFD) solver is used to accurately calculate the unsteady fluid dynamics over a relatively small region near the surface, and an acoustics code based on the Ffowcs Williams and Hawkings [10] (FW–H) equation computes the acoustic-field generated by the previously calculated unsteady flow field.

As a first step in this feasibility analysis, the flow around a circular cylinder with unsteady vortex shedding is analyzed. Although the noise produced by unsteady vortex shedding is different from that produced by sharp trailing edges, both flows involve the formation of wakes. Prior uses of codes based on the FW–H equation have not investigated the situation where a permeable integration surface cuts through the wake. We demonstrate that the FW–H equation, rather than a Kirchhoff formulation, is appropriate for this condition.

Following successful resolution of the wake issue, the numerical solution of the FW–H equation is compared to the exact analytical solution found by Crighton for a line vortex travelling around the edge of a flat plate. This test problem confirms the ability of the FW–H acoustics code to correctly predict the propagation of acoustic signals arising from scattering processes.

Finally, a model problem involving vortices convecting past the sharp trailing edge of an airfoil is investigated. The vortices approximate large-scale flow structures present in turbulent flows. The unsteady flow field from the CFD calculation is used as input for the FW–H acoustics code. Noise spectra, directivity, and Mach number scaling are obtained without the introduction of empirical constants.

2. COMPUTATIONAL TOOLS

2.1. THE COMPUTER CODE CFL3D

The computer code CFL3D [11, 12] is used to compute the unsteady flow field. The CFL3D code was developed at NASA Langley Research Center to solve the three-dimensional, time-dependent, thin-layer (in each co-ordinate direction) Reynolds-averaged Navier–Stokes (RANS) equations using a finite-volume formulation. The code uses upwind-biased spatial differencing for the inviscid terms and flux limiting to obtain smooth solutions in the vicinity of shock waves. The viscous derivatives, when used, are computed by second order central differencing. Fluxes at the cell faces are calculated by the flux-difference-splitting method of Roe [13]. An implicit three-factor approximate factorization method is used to advance the solution in time. Patched grid interfaces, implemented by Biedron and Thomas [14], are used at several of the zone boundaries to reduce the total number of grid points in the calculation.

The time-dependent version of CFL3D uses subiterations to obtain second order temporal accuracy. The τ-TS subiteration option [15] is exercised in this work. In this option, each of the subiterations is advanced with a pseudotime step. This approach facilitates a more rapid convergence to the result at each physical time step. In our calculations, four subiterations are used for each physical time step.

Although the low-order numerical techniques used in CFL3D are a possible source of concern in acoustic applications, recently Rumsey *et al.* [16] successfully used CFL3D to compute the generation and nearfield propagation of acoustic modes through a ducted-fan engine. Their work demonstrated that CFL3D can calculate the unsteady compressible flow, including the acoustics, when appropriate grids and time steps are used.

2.2. FFOWCS WILLIAMS AND HAWKINGS CODE

The Ffowcs Williams and Hawkings [10] equation is the most general form of the Lighthill acoustic analogy and when provided with input of unsteady-flow conditions, is appropriate for computing the acoustic field. The equation is derived directly from the equations of conservation of mass and momentum. Following Brentner and Farassat [17], the FW–H equation may be written in differential form as

$$\Box^2 c^2 \rho'(\mathbf{x}, t) = \frac{\partial^2}{\partial x_i \, \partial x_j} [T_{ij} H(f)] - \frac{\partial}{\partial x_i} [L_i \delta(f)] + \frac{\partial}{\partial t} [(\rho_0 U_n) \delta(f)], \tag{1}$$

where $\Box^2 \equiv (1/c^2)\partial^2/\partial t^2 - \nabla^2$ is the wave operator, c is the ambient speed of sound, t is the observer time, ρ' is the perturbation density, ρ_0 is the ambient density, $f = 0$ describes the integration surface, $f < 0$ being inside the integration surface, $\delta(f)$ is the Dirac delta function, and $H(f)$ is the Heaviside function. The quantities U_i and L_i are defined by

$$U_i = \left(1 - \frac{\rho}{\rho_0}\right) v_i + \frac{\rho u_i}{\rho_0} \tag{2}$$

and

$$L_i = P_{ij} \hat{n}_j + \rho u_i (u_n - v_n). \tag{3}$$

In the above equation, ρ is the total density, ρu_i, the fluid momentum, v_i is the velocity of the integration surface $f = 0$, and P_{ij} is the compressive stress tensor. For an inviscid fluid, $P_{ij} = p' \delta_{ij}$ where p' is the perturbation pressure and δ_{ij} is the Kronecker delta. The subscript n indicates the component of velocity in the direction normal to the surface, and $\hat{n}_j$ is the unit normal.

In contrast to the FW–H equation, the Kirchhoff equation is derived from the acoustic wave equation. It is valid only in the region of the flow where the wave equation is the appropriate governing equation. As shown by Brentner and Farassat [17], the FW–H equation can be rewritten in a form similar to the Kirchhoff equation with additional terms on the right-hand side. These additional terms are negligible in the region where the wave equation is the appropriate governing equation, but not near a body in motion.

An integral solution to the FW–H equation (1) can be written in terms of the acoustic pressure $p' = c^2 \rho'$ in the region $f > 0$. Utilizing formulation 1A of Farassat [18, 19], the integral representation is

$$p'(\mathbf{x}, t) = p'_T(\mathbf{x}, t) + p'_L(\mathbf{x}, t) + p'_Q(\mathbf{x}, t), \tag{4}$$

where

$$4\pi p'_L(\mathbf{x}, t) = \int_{f=0} \left[\frac{\rho_0 (\dot{U}_n + U_{\dot{n}})}{r(1 - M_r)^2} \right]_{\text{ret}} \mathrm{d}S + \int_{f=0} \left[\frac{\rho_0 U_n (r \dot{M}_r + c(M_r - M^2))}{r^2 (1 - M_r)^3} \right]_{\text{ret}} \mathrm{d}S \tag{5}$$

and

$$4\pi p'_L(\mathbf{x}, t) = \frac{1}{c}\int_{f=0}\left[\frac{\dot{L}_r}{r(1-M_r)^2}\right]_{\text{ret}} \mathrm{d}S + \int_{f=0}\left[\frac{L_r - L_M}{r^2(1-M_r)^2}\right]_{\text{ret}} \mathrm{d}S$$

$$+ \frac{1}{c}\int_{f=0}\left[\frac{L_r(r\dot{M}_r + c(M_r - M^2))}{r^2(1-M_r)^3}\right]_{\text{ret}} \mathrm{d}S. \tag{6}$$

Here the dot indicates a time derivative, $L_M = L_i M_i$, where M_i is the velocity of the surface $f = 0$ normalized by the ambient sound speed, r is the distance from a source point on the surface to the observer, and the subscript r indicates the projection of a vector quantity in the radiation direction. The quadrupole term $p'_Q(\mathbf{x}, t)$ can be determined by any method that is currently available (e.g., reference [20]). The term p'_Q accounts for all quadrupoles outside of the integration surface (i.e., $f > 0$). In the current work, p'_Q is neglected.

The numerical solution to equations (4)–(6) was implemented by Brentner and Farassat [17] in the code known as FW–H/RKIR. The FW–H/RKIR code is based upon a rotating Kirchhoff formulation for helicopter rotors developed by Lyrintzis and his colleagues [21, 22]. For this work, the code was modified to remove helicopter blade motions. A preprocessor code was written to perform the task of interpolating the CFD data from CFL3D at each time step onto the integration surface used by FW–H/RKIR. The integration surfaces used here are not appropriate for Kirchhoff integration because they are located in the near field, rather than in the linear acoustic field. The preprocessor also replicated the two-dimensional (2-D) surface data in the spanwise direction to simulate three-dimensional (3-D) data. The integration surface used in the FW–H computations did not include the ends of the cylindrical integration surface. More information about the FW–H/RKIR code is provided by Brentner and Farassat [17].

3. THE MODEL PROBLEMS

3.1. THE CYLINDER

The first model problem consists of a circular cylinder in a cross-flow. Brentner *et al.* [23] examined this general problem using similar computer codes. In their work, the integration surface for the FW–H code was chosen coincident with the physical surface. In the present study, the integration surface is not restricted to the physical surface.

In this work, a cylinder with a diameter D of 0·019 m and a span (of replicated two-dimensional data) that extends $40D$ (0·76 m) is used. The free-stream Mach number is 0·2. Viscous two-dimensional calculations have been performed with a Reynolds number of 1000 based on free-stream velocity and cylinder diameter. The acoustic signal is observed at a position $128D$ (2·432 m) from the cylinder center along a line mutually perpendicular to the free-stream direction and the

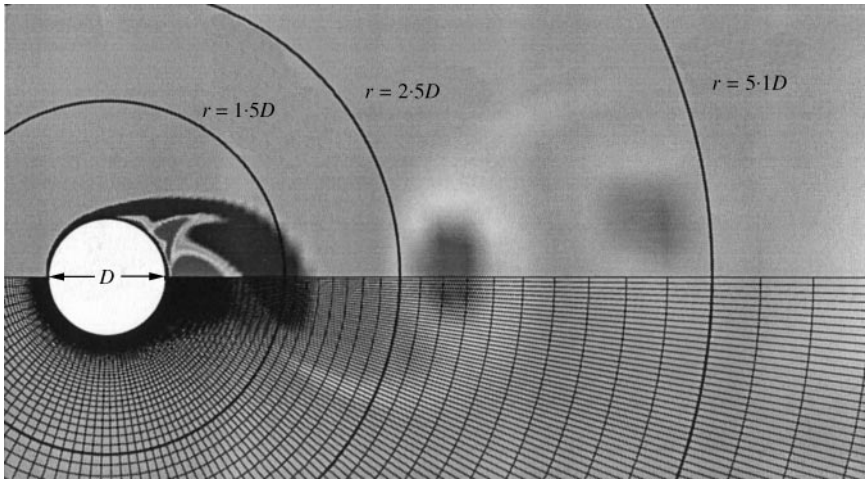

Figure 1. Vorticity field computed from CFD. FW–H integration surfaces are at $r = 0{\cdot}5D$, $r = 1{\cdot}5D$, $r = 2{\cdot}5D$, and $r = 5{\cdot}1D$.

cylinder axis. The CFD grid about the cylinder is stretched both radially and circumferentially in such a way that more points are concentrated in the cylinder wake than upstream of the cylinder. FW–H integration surfaces are on the cylinder surface ($0{\cdot}5D$) and at radial distances from the cylinder axis of $1{\cdot}5D$, $2{\cdot}5D$, and $5{\cdot}1D$. Figure 1 renders an instantaneous vorticity field obtained from the CFD calculation with a superimposed grid distribution on the lower portion of the figure. The positions of the FW–H integration surfaces are indicated in the upper portion of the figure. Figure 2(a) shows the computed pressure signals at the observer for the different integration surfaces using a Kirchhoff formulation and Figure 2(b) shows the results obtained with the FW–H formulation. The computed acoustic signal is not expected to vary with the integration surface location because at the low Mach number of this flow, Cox [24] has shown that the contribution of p'_Q is insignificant compared with the loading contribution. The use of an integration surface that cuts through the cylinder wake does not appear to adversely affect the results obtained with the FW–H formulation. The variations observed show small conflicting effects as the integration surface $f = 0$ is expanded to include more of the flow. The more extensive integration surfaces implicitly include more of any p'_Q contributions by enclosing them within the integration surface, but the more extensive integration surfaces also show the effects of increased numerical diffusion as the grid coarsens. However, these variations are very small compared with the results of Figure 2(a), in which the pressure computed with a standard Kirchhoff formulation for the same problem with the same integration surfaces varies wildly.

3.2. LINE VORTEX AROUND AN EDGE

The second model problem relates to the acoustic radiation from a 2-D vortex filament moving around the edge of a half-plane. This problem was solved

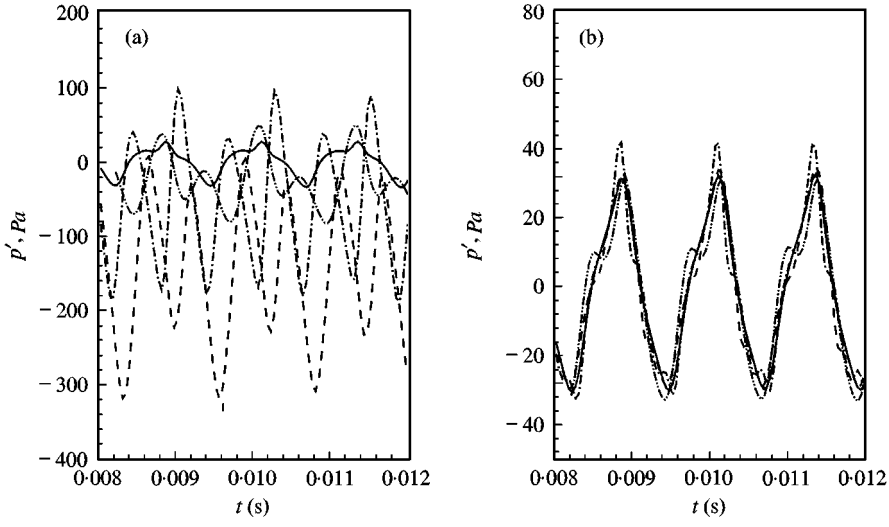

Figure 2. Acoustic signals computed for various integration surfaces that correspond to those indicated in Figure 1. Integration surface at: ——, $r = 0{\cdot}5D$; – – – – –, $r = 1{\cdot}5D$; – · – · –, $r = 2{\cdot}5D$; – ·· – ·· –, $r = 5{\cdot}1D$. (a) Computations with Kirchhoff scheme. (b) Computations with FW–H scheme.

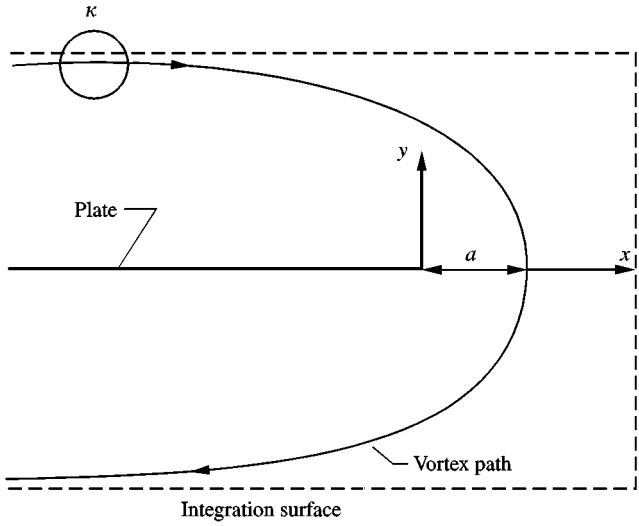

Figure 3. Line vortex moving around semi-infinite plate.

analytically by Crighton [6] for low Mach numbers. Below we first summarize Crighton's analysis and then discuss the application of the FW–H acoustic code to the problem.

The incompressible motion of a line vortex around a rigid semi-infinite plate is determined by potential-flow theory. Figure 3 shows the salient features of the problem. A vortex of strength κ moves along the indicated path around the edge of

the plate. The point of closest approach occurs at $x = a$, $y = 0$, at which point the vortex moves with speed $u = \kappa/4\pi a$. With the path of the vortex determined, the fluid is then assumed to be slightly compressible, that is, $M \equiv u/c \ll 1$. The spatial co-ordinates are rescaled by multiplication with the Mach number M and the limit taken as $M \to 0$. The velocity potential for the incompressible inner solution is matched to the velocity potential for the slightly compressible outer solution, and a radiation condition is applied to the outer solution at infinity. The resultant velocity potential, expressed in non-dimensional form is,

$$\phi(x, y, t) = \frac{4^{3/4}}{[(r-t)^2 + 4]^{1/4}} \frac{M^{1/2} \sin(\theta/2)}{r^{1/2}}, \tag{7}$$

where r is the non-dimensional distance from the edge and θ is the angle measured relative to the positive x-axis.

To test the ability of the FW–H acoustic code to compute a scattered acoustics field, the exact acoustic solution to the problem, equation (7), with $M = 0{\cdot}01$, is used to establish flow conditions on an integration surface as shown in Figure 3. Note that the vortex trajectory is entirely within the integration surface. The full extent of the integration surface is $-200a \leqslant x \leqslant 2a$, $-2a \leqslant y \leqslant 2a$, $-500a \leqslant z \leqslant 500a$. Here z is the spanwise co-ordinate. On the $x = -200a$ face, the value of the pressure and wall-normal velocity at $y = 0$ is ambiguous because of a phase shift (between the upper and lower surfaces). Careful choice of integration points avoided the ambiguity. Later investigation revealed that the contributions to the acoustic signal from the $x = -200a$ face were so small that the face could be neglected without producing a noticeable change in the solution. Because of the low speed of the vortex as compared with the speed of sound, the time required for the vortex to move from directly above the edge of the plate to directly below the edge is sufficient for an acoustic wave to travel $200a$. If that time span approximates the time of the vortex interaction with the edge, then we should expect a streamwise domain extent of at least $200a$ to be required. Figure 4 shows a comparison between the exact solution derived from equation (7) and the numerically computed solution for observers at a radius of $50a$ from the edge. To achieve these results, 250 cells are used to span the x direction, 50 cells are used to span the y direction, and 2500 cells are used to span the z direction. Numerical experimentation revealed a steady degradation of the results with reduction in the number of grid cells. Significant reduction in the domain extent in either the x or z direction also degrades the accuracy of the computed results. The results suggest that the FW–H integration surface must extend over a significant portion of the plate because the no-penetration boundary condition makes much of the plate appear to radiate. Hence, the integration surface must extend to encompass all of these significant acoustic sources. The extensive integration domain required in the z direction is surprising. However, further analysis suggests that the oscillatory behavior of the integrand as a function of z results in the slow convergence to the 2-D solution. In fact, the difficulties with the z integration could be overcome by performing the z integration analytically by using the method of stationary phase. Although such

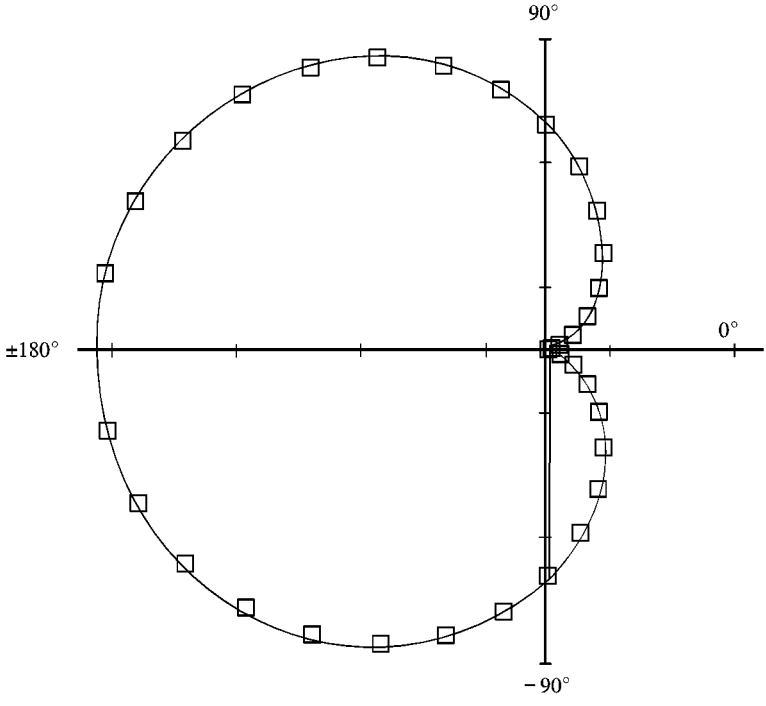

Figure 4. Acoustic pressure squared at $r = 50a$ for line vortex moving around semi-infinite plate with $M = 0{\cdot}01$. —— theory, □ FW–H.

an option might be useful for this particular model problem, its extension to more complex problems is more difficult. In addition, our longer-term goal is to use the FW–H acoustics code for 3-D problems, so performing the z integration numerically is more consistent with our expected future approach.

Because an exact incompressible solution is available for the vortex, this model problem also affords us the opportunity to explore conditions under which the incompressible solution could be used directly as input into the FW–H acoustics code. The integration surface for these tests is a surface displaced $10^{-5}a$ above and below the plate joined by a small circular region of radius $0{\cdot}01a$ near the plate edge at $x = 0$. This computed solution displays a dipole-like directivity pattern centered on the plate edge, and not the cardioid shown in Figure 4. For cases in which noise radiates from a region that is not spatially compact, as in this problem, these results show that the use of the incompressible data to obtain integration surface quantities for use in a FW–H acoustics code leads to an incorrect solution if some method is not first introduced to account for a finite propagation time.

3.3. THE AIRFOIL

We now address the edge noise problem by considering an airfoil with vortices convecting past its trailing edge. The calculations were performed using the inviscid

option of CFL3D. The inviscid option was chosen to avoid having Reynolds number variations between runs with different Mach numbers. The small amount of numerically induced viscosity was expected to be sufficient to produce vortex roll-up shortly downstream of the vortex-generator plate, but otherwise not to interfere much with the flow past the airfoil trailing edge. The observed effects are discussed more fully below.

3.3.1. *Geometry*

In this model problem we have flow over a 2·6% thickness NACA 00 series airfoil. The cross-section of the particular airfoil used is shown in Figure 5(a). The chord C is chosen to be 1 m. For the purposes of the acoustic calculation, the span of the airfoil is twice the chord, or 2 m. The thin airfoil enables a larger range of subsonic Mach numbers to be studied without the presence of transonic flow effects. The circle indicates the region near the trailing edge of the airfoil that is magnified in Figure 5(b). At 98% of the chord, a flat plate is introduced perpendicular to the flow. The flat plate extends from $0{\cdot}0015C$ (1·5 mm) to $0{\cdot}0025C$ (2·5 mm) above the airfoil chordline. In the presence of flow, vortices roll up just downstream of the flat plate, alternately near the plate's top and bottom edges. The placement of the vortex-generator plate is a compromise between conflicting requirements. The plate needs to be sufficiently far from the trailing edge so that it does not interfere with the trailing edge scattering phenomenon. However, the realities of numerical dissipation and the need for extremely fine grid resolution to capture the shed vortices dictate that the distance from the vortex-generator plate to the trailing edge be minimized. The height of the plate $L = 1$ mm ensures that the acoustic wavelength λ of the dominant frequency scattered by the trailing edge is much smaller than the chord (i.e., $\lambda/C \ll 1$). The dominant shedding frequency f_s is related to the plate height via the Strouhal number $\mathrm{St} = Lf_s/U_0$ where U_0 is the free-stream velocity. The dominant acoustic frequency is expected to equal the vortex shedding frequency. By expressing the acoustic wavelength in terms of f_s and the sound speed c, we can relate λ/C to the Strouhal number, the Mach number $M_0 = U_0/c$, and the normalized flat plate height L/C by

$$\frac{\lambda}{C} = \frac{L/C}{\mathrm{St} \cdot M_0}. \tag{8}$$

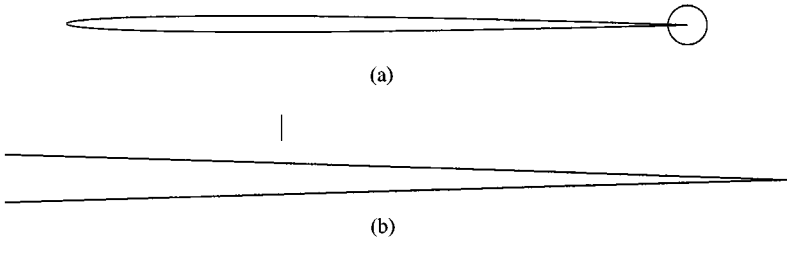

Figure 5. View of airfoil geometry. (a) Airfoil section. (b) Magnified view of the region encircled in Figure 5(a), showing airfoil trailing edge and vortex-generator plate.

With an estimated Strouhal number between 0·1 and 0·2 and a free-stream Mach number of 0·2, the chosen $L/C = 0{\cdot}001$ satisfies the constraint $\lambda/C \ll 1$ even with moderate variations in the Strouhal number and the Mach number.

3.3.2. *CFD grid*

The CFD grid requirements are driven by the unsteady flow. Extremely fine gridding is require downstream of the vortex-generator plate to resolve the complex physics associated with the vortex dynamics leading to acoustic scattering at the edge. Because the noise radiates from a region that is not spatially compact, the grid needs to resolve the dominant acoustic waves radiated over a significant portion of the surface of the airfoil. Far from the airfoil, the only important requirement is that no reflections from boundaries interfere with the calculation. To meet these requirements, we implemented a seven-zone, patched grid. Each zone contains a stretched, and sometimes slightly skewed, Cartesian mesh. The use of Cartesian meshes with patched interfaces at the zone boundaries make grid modifications particularly easy. The finest grid used had the zonal grid resolutions indicated in Figure 6. Figure 7 shows a magnified view of the grid in the vicinity of the bluff body. For clarity, only every fourth grid line is shown in Figure 7. The computational domain extends $2C$ upstream of the leading-edge, $2C$ downstream of the trailing edge, and $2C$ above and below the airfoil chordline. The grid downstream of the trailing edge is stretched sufficiently to diffuse the vortices long before they encounter the computational domain outflow boundary.

At the upstream boundary, free-stream conditions are imposed. Above and below the airfoil, farfield conditions for the normal velocity and the speed of sound are obtained from two locally 1-D Riemann invariants. The downstream outflow boundary employs simple extrapolation.

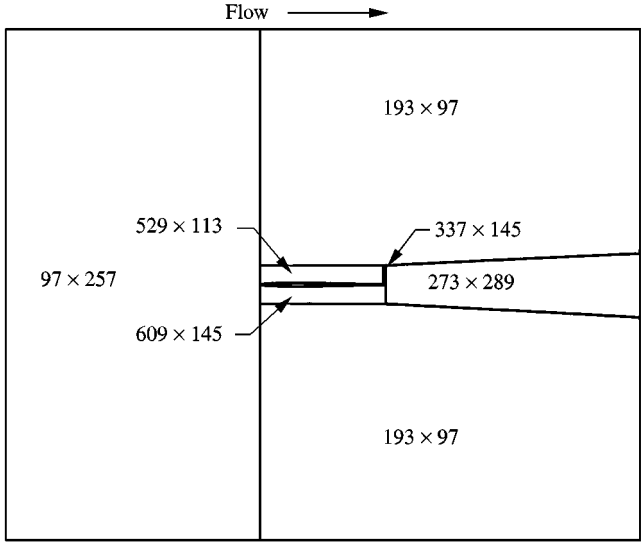

Figure 6. Resolution in 7-zone grid.

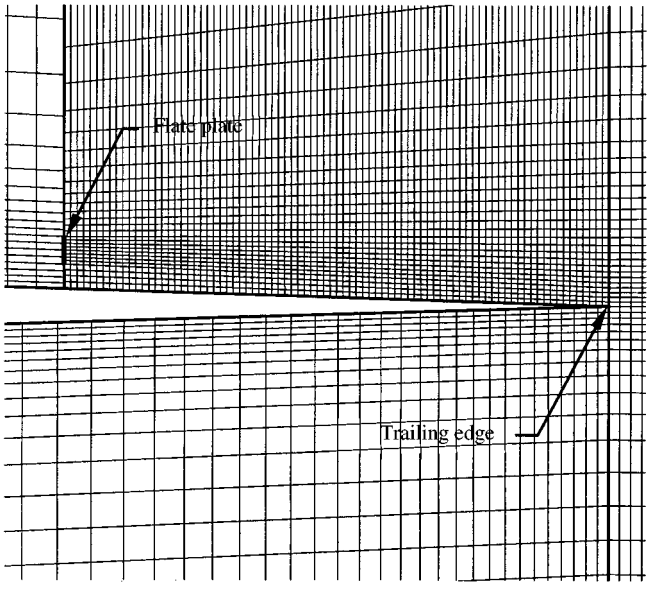

Figure 7. Magnified view of grid in vicinity of bluff body. Actual flat plate has zero thickness. Every fourth grid line is shown.

The calculations are performed on two coarser grids, each successively halving the grid resolution in each direction. The two coarser grids are run with a time step of $0{\cdot}001C/c$. Three cases with the finest grids were run with the time step varying from $0{\cdot}001C/c$ to $0{\cdot}00025C/c$.

3.3.3. *Effects of varying grid resolution*

Some important changes in the overall flow features occur as the CFD grid resolutions and time step are varied. As an indication of these changes, Figure 8 shows the spectra of the pressure coefficient for the different resolutions at a location directly under the vortex-generator plate. At the lowest resolution, the spectrum is dominated by the peaks at the shedding frequency and its harmonics. Increasing the grid resolution fills the spectrum more fully and shifts the shedding frequency slightly lower. Similarly, the spectrum becomes fuller and the dominant frequency shifts slightly lower as the time step is decreased. Observations of the time-dependent flow data revealed that either increased grid resolution or a finer time step results in more vortex amalgamation in the region between the vortex-generator plate and the airfoil trailing edge.

In hindsight, the variation of the results with grid resolution and time step should have been expected. Originally, an inviscid calculation was chosen in order to avoid Reynolds-number variations for runs with different Mach numbers. With no physical viscosity in the calculations, dispersion and dissipation are governed by the numerical truncation error, which is expected to be small in the region between the vortex-generator plate and the airfoil trailing edge. Unfortunately, the process

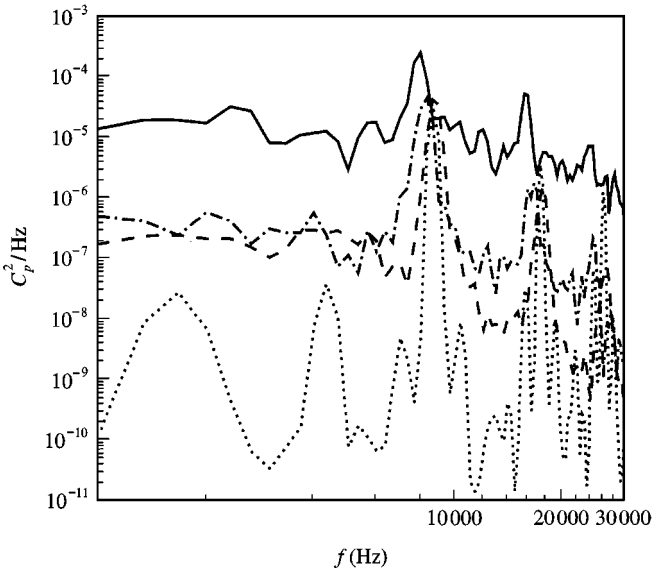

Figure 8. Spectra of pressure coefficient under vortex-generator plate for different grid resolutions with $M = 0{\cdot}2$; · · · · · ·, low resolution: – – – – –, medium resolution; – · – · – ·, high resolution; ——, high resolution with fine time step.

of vortex amalgamation is sensitive to the physical viscosity. Hence, in the numerically simulated cases, even small differences in the numerically introduced effective viscosity produce noticeable changes in the results. Results at different Mach numbers are therefore also at different effective Reynolds numbers—the very effect that we originally sought to avoid. In part, because of these difficulties, the results obtained are useful in that they provide guidance as to the problems and capabilities of the hybrid calculation procedure for complex flows. In future work, the effects of including viscosity and turbulence modelling should be investigated.

In what follows, all results have been obtained by using the finest grid with the smallest time step. Based upon the acoustic wavelength for an 8000 Hz signal (roughly the peak frequency in Figure 8) and the maximum grid spacing over the airfoil, slightly more than 13 grid cells per wavelength were used. However, approximately 60% of the grid cells adjacent to the airfoil surface provided better than 25 points per wavelength and the grid near the trailing edge contained more than 700 points per wavelength.

3.3.4. *General flow features*

Figure 9 shows vorticity magnitude contours in the vicinity of the trailing edge at a single time step. The circular concentrations of vorticity indicate the individual vortices that constitute the unsteady Karman vortex street downstream of the vortex-generator plate. Vortices are shed alternately from opposite ends of the vortex-generator plate. At a Mach number of 0·2, the Strouhal number of the vortex shedding is approximately 0·12, based on the height of the flat-plate vortex

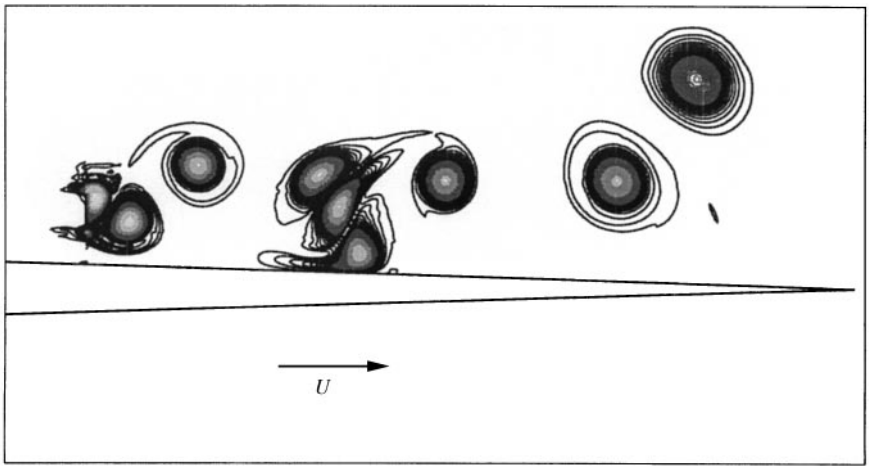

Figure 9. Instantaneous vorticity magnitude contours in vicinity of trailing edge for $M = 0{\cdot}2$ case. Approximately 2% of aft portion of airfoil is shown.

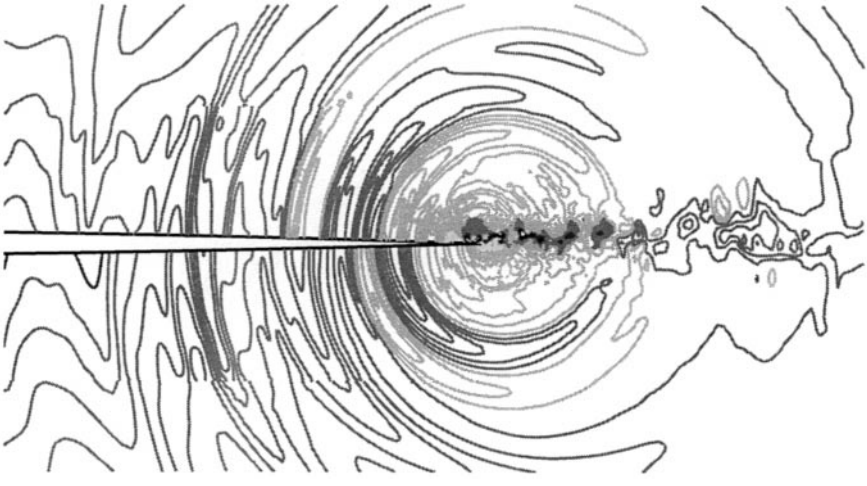

Figure 10. Instantaneous pressure contours (with restricted min–max limits) over approximately 40% of airfoil for $M = 0{\cdot}2$ case.

generator and the free-stream speed. At a Mach number of 0·4, the Strouhal number of the vortex shedding is approximately 0·13. If based on the actual convection speed of the vortices, the Strouhal number would be somewhat larger. The frequency of the vortices convecting past the trailing edge is less distinct because the vortices shed from the vortex-generator plate often pair and interact with neighboring vortices, as shown in Figure 9.

Figure 10 shows instantaneous pressure contours in the vicinity of the trailing edge of the airfoil. The contours have been restricted to a narrow range about the mean pressure so that the acoustic waves emanating from the trailing edge are more

visible. The figure clearly shows the upstream propagation of acoustic waves that results from the vortices passing close to the airfoil trailing edge.

3.3.5. *Acoustics*

The FW–H code computes the acoustic field generated by the unsteady aerodynamic flow field. In this work we explore the use of two integration surfaces, one on the airfoil body and a second approximately 1% of the chord off the airfoil. Figure 11(a) shows the off-airfoil-body integration surface together with the airfoil body. Figure 11(b) shows a close-up of the trailing-edge area. The region enclosed by the off-airfoil-body surface includes all of the vortices between the bluff body and trailing edge as well as the first few vortices in the wake region. We observe that the resolution of the integration surface is least critical (for numerical reasons) when a straight line is used to close the downstream end of the surface. Our tests indicate that increasing the number of points on the integration surface (via interpolation of the CFD data) results in only small changes in the observed acoustic signals.

The farfield signals are obtained at several observer locations. For Figures 12–15, the observers are all located $10C$ (10 m) from the trailing edge of the airfoil. Figure 12 shows spectra of the acoustic signals for several observer positions. The angular measurements are increasingly positive for counterclockwise rotations, with 0° being directed downstream. The figure shows greatly reduced noise radiation directly upstream and directly downstream.

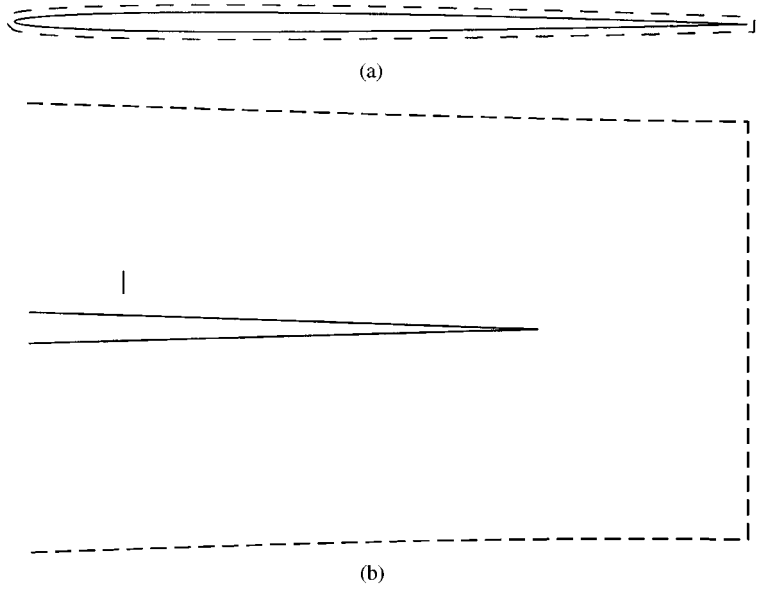

Figure 11. Integration surfaces used for acoustics calculations. Short vertical line indicates location of vortex-generator plate: ——, on-airfoil-body integration surface; – – – – –, off-airfoil-body integration surface. (a) View of complete integration surfaces. (b) Close-up of trailing-edge region.

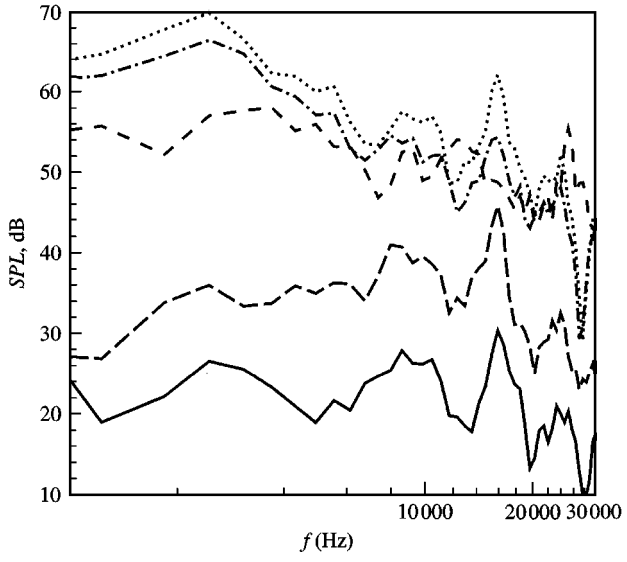

Figure 12. Spectra of acoustic-signals (referenced to 20 μPa) for observers located 10C from trailing edge of airfoil; on-airfoil-body integration surface used, $M = 0{\cdot}2$. Observers located at: ——, 0°; – – – – –, 45°; – · – · –, 90°; · · · · · ·, 135°; — — —, 180°.

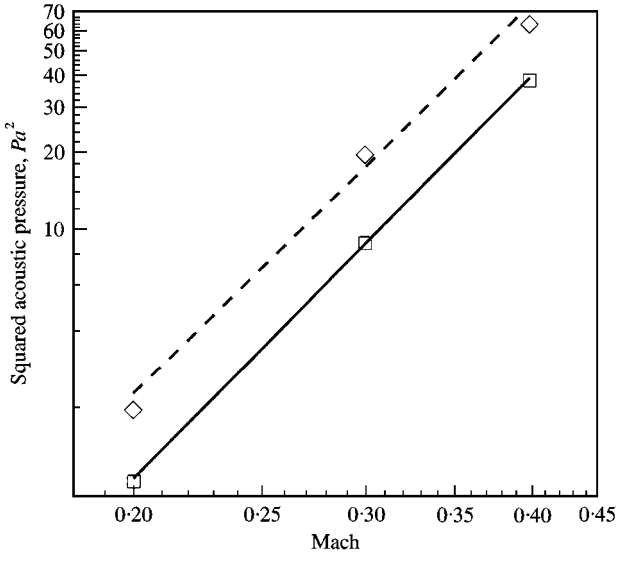

Figure 13. Variation in mean square acoustic pressure versus Mach number: □, data for 30°; ——, least-squares fit for 30°; ◇, data for 45°; – – – – –, least-squares fit for 45°.

Integration of each acoustic spectrum over the frequencies provides the mean square acoustic pressure. Variation of the mean square acoustic pressure as a function of Mach number is plotted in Figure 13. The symbols show the data, and the lines are linear least-squares fits to the logarithm of the data. For an observer at 30°, the mean square pressure varies as the 5·2 power of Mach number. For an

observer at 45°, the data do not align quite so well, but least-squares regression indicates variation with the 5·0 power of Mach number. Theoretically, we expect the scaling law to be M^4 for the 2-D case of vortices convecting past the edge of a semi-infinite rigid plate and we assume that a similar result will occur for the airfoil of finite chord, as used in our problem. Currently, we do not possess a general theory for the airfoil of finite chord. This scaling would be obtained by assuming complete coherence in the spanwise direction and integrating the result of Ffowcs Williams and Hall [3] for infinitesimal Mach numbers along the infinite span. In addition to the finite Mach numbers used in the CFD (as opposed to the infinitesimal Mach number of the theory), another source of the discrepancy between the theoretical M^4 scaling law and the value of $M^{5\cdot2}$ obtained from the computations is that the root mean square (r.m.s.) fluctuating velocity above the airfoil does not vary linearly with free-stream velocity, but instead varies as $M^{1\cdot34}$. Accounting for the actual r.m.s. fluctuating velocity, a scaling of $M^{5\cdot36}$ is implied, which is in close agreement with our computationally observed scaling of $M^{5\cdot2}$. We note that this close agreement has only been obtained by neglecting the Doppler corrections as predicted by Howe [7] for the semi-infinite flat plate. Our data do not appear to support the effect of significant Doppler correction terms, at least up to $M = 0{\cdot}4$.

The directivity of the acoustic signals is shown in Figures 14(a) and (b). To show the results for all three Mach numbers on the same plot, the mean square pressures are scaled with $M^{-5\cdot2}$. Figure 14(a), shows the case in which the integration surface is on the airfoil body. The null regions in the vicinity of 0 and 180° are typical of acoustic scattering over a finite streamlined body (cf. Figure 3.14 of Wagner *et al.* [9]). Note that the scaling collapses the results for the different Mach numbers reasonably well. Figure 14(b) shows the results for cases in which the off-airfoil-body integration surface is used. The data still collapse satisfactorily in

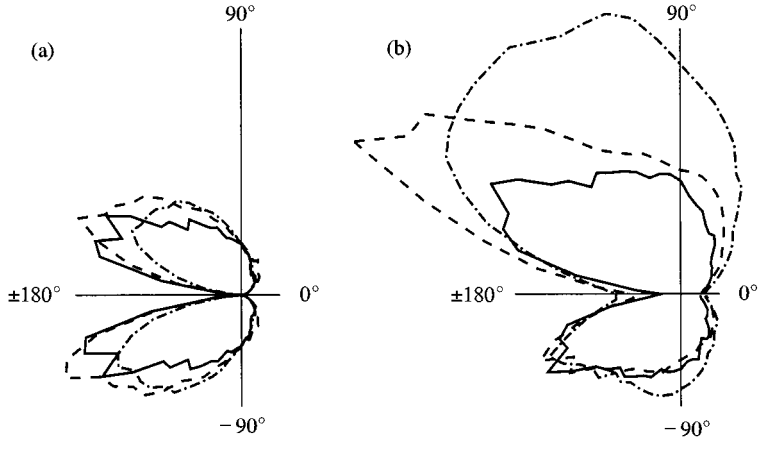

Figure 14. Scaled directivity of squared pressure for observers 10 chord lengths from trailing edge; squared pressure is scaled with $M^{-5\cdot2}$. Both (a) and (b) use the same scale. ——, $M = 0{\cdot}2$; – – – – –, $M = 0{\cdot}3$; – · – · –, $M = 0{\cdot}4$. (a) On-airfoil-body integration surface. (b) Off-airfoil-body integration surface.

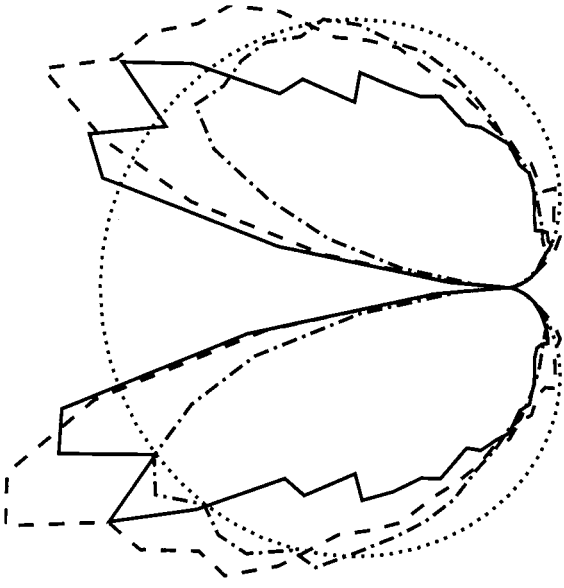

Figure 15. Scaled squared pressure with cardioid included; squared pressure is scaled with $M^{-5\cdot2}$: ––, $M = 0\cdot2$; – – – – –, $M = 0\cdot3$; – · – · –, $M = 0\cdot4$; · · · · · ·, cardioid.

the region under the airfoil, but not so well above the airfoil. The upper-lower asymmetry in Figure 14(b) suggests that the shedding of the vortices from the vortex-generator plate produces noise that radiates predominantly above the airfoil. The noise produced by the vortex-generator plate is not included in any of the edge-scattering theories. The noise that radiates below the airfoil is likely to be dominated by the field scattered by the trailing edge.

In Figure 15, we compare the directivity of the acoustic signal to the $\sin^2(\theta/2)$ directivity for an acoustic source near the edge of a rigid half-plane. The amplitude of the $\sin^2(\theta/2)$ prediction is matched with the amplitude of the computed acoustic signal at 30^0. All of the acoustic signals in Figure 15 are computed using the on-airfoil-body integration surface. For all three Mach numbers, the agreement with the theoretically predicted pattern is very good for $-45^\circ < \theta < 45^\circ$. As the angle increases, diffraction from the leading edge is expected to degrade agreement with the semi-infinite plate solution. In addition, the coarser grid resolution on the middle and upstream portions of the airfoil probably affect the computed directivity adversely.

4. CONCLUSIONS

Three model problems were investigated to address the fitness of the hybrid CFD/FW–H method for predicting acoustics in complex flow fields.

The first model problem involved the sound generated by vortex shedding from a circular cylinder with axis normal to the flow. We showed that the FW–H approach provides consistent prediction of acoustic signals for integration surfaces

both on and off the body, even when the off-airfoil-body integration surfaces intersected the cylinder wake. In contrast, a Kirchhoff formulation that uses the same integration surfaces gives erratic results, with acoustic signals varying by more than an order of magnitude.

The second model problem sought to confirm the ability of the FW–H approach to predict the acoustic propagation associated with edge scattering. We chose to study Crighton's [6] exact model problem of a line vortex travelling around the edge of a rigid half-plane under its own induced velocity field. We found that the FW–H approach correctly predicts the farfield noise, provided that the integration surface extends sufficiently upstream and laterally. The upstream extent should be far enough to include the passage of acoustic waves produced during the time that the vortex is in the vicinity of the half-plane edge. The spanwise extent needs to be great enough to converge a slowly varying oscillatory integral, which results from attempting to compute a strictly 2-D case in a 3-D acoustic computation. As an aside, we found that for cases in which the noise radiates from a region that is not spatially compact the incompressible results cannot be used directly to provide unsteady flow data on the integration surface.

Finally, we investigated using CFD to compute the flow of vortices convecting past the trailing edge of an airfoil and the FW–H approach to predict the noise produced. Because vortex generation and vortex interaction are inherently viscous phenomena, changes in grid resolution (and the associated changes in the small amount of artificial viscosity in the inviscid CFD), alter the character of the flow field. In spite of this, many of the expected acoustic features of the flow are observed when the time-accurate CFD data are used as input for a FW–H analysis. The general directivity pattern is similar to that illustrated in reference [9]. In fact, the half-plane prediction of a $\sin^2(\theta/2)$ dependency of the intensity is observed in the quadrant around the trailing edge. Velocity scaling of the computed acoustic signal suggests an approximate $M^{5\cdot2}$ dependency, although extension of the Ffowcs Williams and Hall [3] analysis for $M \to 0$ to 2-D configurations implies an M^4 dependency. Accounting for the non-linear dependence of the r.m.s. velocities at the trailing edge with free-stream Mach number improves the agreement between the calculations and the theoretical predictions. Without a complete theory that includes the finite chord of the airfoil and the finite Mach numbers of the flows, the current agreement is as good as we can expect.

ACKNOWLEDGMENTS

The authors thank Drs Christopher Rumsey and Robert Biedron for many useful suggestions in the use of CFL3D.

REFERENCES

1. M. J. Lighthill 1952 *Proceedings of the Royal Society* A**221**, 564–587. On sound generated aerodynamically, I: general theory.
2. M. J. Lighthill 1954 *Proceedings of the Royal Society* A**222**, 1–32. On sound generated aerodynamically, II: turbulence as a source of sound.

3. J. E. Ffowcs Williams and L. H. Hall 1970 *Journal of Fluid Mechanics* **40**, 657–670. Aerodynamic sound generation by turbulent flow in the vicinity of a scattering half plane.
4. N. Curle 1955 *Proceedings of the Royal Society* **231**, 505–514. The influence of solid boundaries upon aerodynamic sound.
5. M. E. Goldstein 1976 *Aeroacoustics*. New York: McGraw-Hill.
6. D. G. Crighton 1972 *Journal of Fluid Mechanics* **51**, 357–362. Radiation from vortex filament motion near a half-plane.
7. M. S. Howe 1978 *Journal of Sound and Vibration* **61**, 437–465. A review of the theory of trailing edge noise.
8. T. F. Brooks and T. H. Hodgson 1981 *Journal of Sound and Vibration* **78**, 69–117. Trailing edge noise prediction from measured surface pressures.
9. S. Wagner, R. Bareiss and G. Guidati 1996 *Wind Turbine Noise*: New York: Springer.
10. J. E. Ffowcs Williams and D. L. Hawkings 1969 *Philosophical Transactions of the Royal Society* A **264**, 321–342. Sound generated by turbulence and surfaces in arbitrary motion.
11. C. Rumsey, R. Biedron and J. Thomas 1997 NASA 112861. CFL3D: Its history and some recent applications.
12. S. L. Krist, R. T. Biedron and C. Rumsey 1997. *CFL3D User's Manual* (*Version* 5). NASA Langley Research Center, Aerodynamic and Acoustic Methods Branch.
13. P. Roe 1981 *Journal of Computational Physics* **43**, 357–372. Approximate Riemann solvers, parameter vectors and difference schemes.
14. R. T. Biedron and J. L. Thomas 1990 *Computing Systems in Engineering* **1**, 563–576. A generalized patched-grid algorithm with application to the F-18 forebody with actuated control strake.
15. C. L. Rumsey, M. D. Sanetrik, R. T. Biedron, N. D. Melson and E. B. Parlette 1996 *Computers and Fluids* **25**, 217–236. Efficiency and accuracy of time-accurate turbulent Navier–Stokes computations.
16. C. L. Rumsey, R. Biedron, F. Farassat and P. L. Spence 1998 *Journal of Sound and Vibration* **213**, 643–664. Ducted-fan engine acoustic predictions using a Navier–Stokes code.
17. K. S. Brentner and F. Farassat 1998 *AIAA Journal* **36**, 1379–1386. An analytical comparison of the acoustic analogy and Kirchhoff formulation for moving surfaces.
18. F. Farassat and G. P. Succi 1983 *Vertica* **7**, 309–320. The prediction of helicopter discrete frequency noise.
19. K. S. Brenter 1986. *Prediction of helicopter discrete frequency rotor noise — a computer program incorporating realistic blade motions and advanced formulation. TM* 87721, NASA Langley Research Center.
20. K. S. Brentner 1997 *Journal of Sound and Vibration* **203**, 87–100. An efficient and robust method for predicting helicopter rotor high-speed impulsive noise.
21. Y. Xue and A. S. Lyrintzis 1994 *AIAA Journal* **32**, 1350–1359. Rotating Kirchhoff method for three-dimensional transonic blade-vortex interaction hover noise.
22. A. S. Lyrintzis, E. K. Koutsavdis, C. Berezin, J. Visintainer and M. Pollack 1995. *American Helicopter Society, Second International Aeromechanics Specialist's Conference*. Kirchhoff acoustic methodology validation and implementation in the tiltrotor aeroacoustic codes (TRAC).
23. K. S. Brentner, J. S. Cox, C. L. Rumsey and B. A. Younis 1997 *Second Computational Aeroacoustics* (*CAA*) *Workshop on Benchmark Problems*, 289–296, *NASA* (*NASA Conference Publication* 3352). Computation of sound generated by flow over a circular cylinder: an acoustic analogy approach.
24. J. S. Cox 1997 *Master's thesis, The George Washington University*. Computation of vortex shedding and radiated sound for a circular cylinder: subcritical to transcritical Reynolds numbers.